Atomization and Sprays, 23 (12): 1079–1101 (2013)

HIGH-FIDELITY SIMULATIONS OF IMPINGING JET ATOMIZATION

Xiaodong Chen,[1] Dongjun Ma,[1] Vigor Yang,[1]* & Stéphane Popinet[2]

[1]*School of Aerospace Engineering, Georgia Institute of Technology, Atlanta, Georgia 30332-0150, USA*

[2]*National Institute of Water and Atmosphere Research, P.O. Box 14-901, Kilbirnie, Wellington, New Zealand*

*Address all correspondence to Vigor Yang
E-mail: vigor.yang@aerospace.gatech.edu

Original Manuscript Submitted: 4/12/2013; Final Draft Received: 10/2/2013

High-fidelity numerical simulations have been performed to study the formation and fragmentation of liquid sheets formed by two impinging jets using an improved volume-of-fluid (VOF) method augmented with several adaptive mesh refinement (AMR) techniques. An efficient topology-oriented strategy was further established to optimize the performance and accuracy of the AMR algorithm. Two benchmark cases pertaining to low- and high-velocity impinging jets are simulated as part of a grid refinement study. Calculated jet dynamics show excellent agreement with experimental observations in terms of the rim shape, droplet size distribution and impact wave structures. Detailed flow physics associated with the temporal evolution and spatial development of the jets are explored over a wide range of Reynolds and Weber numbers. A realistic rendering post-processing using a ray-tracing technique is performed to obtain direct insight to the flow evolution. Special attention is paid to the dynamics of the impact wave which dominates the atomization of the injected liquid. The work appears to be the first systematic numerical study in which all the flow patterns formed by impingement of two liquid jets are obtained. Fine structures are captured based on their characteristic length scales. Various atomization modes, from stable to highly unstable, are resolved with high fidelity.

KEY WORDS: *numerical simulation, impinging jets, VOF, primary atomization*

1. INTRODUCTION

Collision between two cylindrical liquid jets is one of the canonical configurations for atomizers used in many propulsion, energy-conversion, material processing, and chemical engineering systems (Lefebvre, 1989; Bayvel and Orzechowski, 1993; Bush and Hasha, 2004; Sutton and Biblarz, 2011). For example, the main propulsion workhorse in the Apollo lunar-landing project (the F-1 engine) employed impinging jet injectors

1044–5110/13/$35.00 © 2013 by Begell House, Inc.

in both the main combustion chamber and the gas generator (Oefelin and Yang, 1993). Impingement of liquid jets is a very efficient method for atomization and mixing, where the dynamic head of the liquid jet is used to destabilize the opposing stream, typically within a short distance from injection. The resultant sheet destabilizes, breaks, and disintegrates into a spray of droplets under the influence of surface-tension, viscous, inertial, and aerodynamic forces. The process eventually leads to fragmentation of the injected liquid into ligaments and droplets (Yang and Anderson, 1995). A rich variety of flow structures, ranging from single oscillating jets at low flow rates to violent disintegration of flapping sheets at higher flow rates, have been observed, depending on the Weber and Reynolds numbers of the jets.

Many experimental and theoretical studies have been performed to explore the underlying mechanisms of impinging jet atomization. Taylor (1960) investigated the formation, breakup, and disintegration of flat sheets by collision of two identical coaxial water jets. Dombrowski and Hooper (1963) conducted extensive experiments to identify the attributes dictating the breakup of high-velocity liquid sheets. Huang (1970) examined the breakup of axisymmetric liquid sheets and analyzed the speeds of asymmetric waves propagating on the sheets. Lin (2003) provided a detailed theoretical review on liquid sheet instability, and introduced the concept of absolute instability for sheet breakup. Heidmann et al. (1957), Bush and Hasha (2004), and Jung et al. (2010) studied various impinging jet flow patterns over a wide range of the Reynolds and Weber numbers. In addition, measurements have been made of sheet thickness (Taylor, 1960; Shen and Poulikakos, 1998), geometry (Taylor, 1960; Ibrahim and Przekwas, 1991; Bremond and Villermaux, 2006; Li and Ashgriz, 2006), and velocity (Choo and Kang, 2003; Li and Ashgriz, 2006; Choo and Kang, 2007), as well as the size distribution of droplets shed from the rim of the liquid sheet (Kang et al., 1995; Bremond and Villermaux, 2006). Several analytical studies were also performed to determine the characteristics of the sheet (Hasson and Peck, 1964; Ibrahim and Przekwas, 1991; Bremond and Villermaux, 2006) and resultant droplets (Bush and Hasha, 2004).

Because of the complexity of such multiscale two-phase flow phenomena, limited literature exists on numerical simulations addressing impinging jet dynamics. Inoue et al. (2008) used the CIP-LSM (CIP-based level-set and MARS) method to simulate the atomization of impinging jets on fixed meshes. The nozzle diameter was resolved by 10 grid points. Flapping liquid sheets were observed, but the grid was too coarse to accurately resolve the ligaments and droplets produced during the fragmentation process. Inoue et al. (2009) simulated the atomization process using a polar coordinate system with the origin placed at the center of the two nozzles. The nozzle diameter was resolved by 40 grid points. The grid size, however, increased dramatically in the downstream region. The effect of the injection velocity profile on the liquid sheet pattern was investigated, but no information was reported about ligament and droplet characteristics. Arienti et al. (2013) studied impinging jet atomization using a combined level-set and volume-of-fluid (CLSVOF) formulation (Sussman et al., 2007), coupled with Lagrangian spray

tracking on a dynamically adaptive, block-structured grid. In their simulations, the cells crossed by the liquid–gas interface were tagged for refinement. Small liquid structures formed during atomization were removed from the Eulerian grid, transformed into Lagrangian particles, and advected downstream as nondeformable spheres. Converged results on droplet size distribution were obtained from simulations with different spatial resolutions.

It is clear from this brief literature survey that there is a need to develop an efficient, high-fidelity methodology which can be used to investigate the physics governing impinging jet dynamics over a wide range of Reynolds and Weber numbers. An improved volume-of-fluid (VOF) method, augmented with several adaptive mesh refinement (AMR) techniques, is developed and implemented to investigate the dynamics of the liquid sheet formed by impingement of two identical jets. In addition, an efficient topology-oriented (TO) strategy was established to optimize the performance and accuracy of the AMR algorithm. Fine structures are captured based on their characteristic length scales. Various atomization patterns, from stable to highly unstable modes, are obtained using this methodology with high fidelity. The mechanisms of impact waves are also revealed and mapped with corresponding theories. To the best of our knowledge, this is the first time that a systematic numerical study has been performed to obtain all the patterns formed by the impingement of two identical liquid jets. More detailed analyses are underway to provide a physical understanding of the instabilities occurring in the liquid sheet and rim formed by the impinging jets. The proposed direct numerical simulation methodology can be applied in the design of impinging jet injectors.

In the following section, the theoretical formulation and numerical framework are summarized. Flow structures of interest are introduced next. This is followed by grid-independence studies on two benchmark problems for low- and high-velocity impinging jets. Finally, the detailed flow physics of jet impingement and ensuing sheet formation and atomization are examined systematically under a wide range of operating conditions.

2. THEORETICAL AND NUMERICAL FRAMEWORK

The formulation is based on three-dimensional conservation equations for an incompressible, variable-density flow with surface tension. They can be written in the following vector form:

$$\partial_t \rho + \nabla \cdot (\rho \boldsymbol{u}) = 0 \tag{1}$$

$$\rho(\partial_t \boldsymbol{u} + \boldsymbol{u} \cdot \nabla \boldsymbol{u}) = -\nabla p + \nabla \cdot (2\mu \boldsymbol{D}) + \sigma\kappa\delta_s \boldsymbol{n} \tag{2}$$

$$\nabla \cdot \boldsymbol{u} = 0 \tag{3}$$

where $\boldsymbol{u} = (u, v, w)$ is the velocity vector, ρ ($\boldsymbol{x}$, t) the fluid density, μ ($\boldsymbol{x}$, t) the dynamic viscosity, and $\boldsymbol{D}$ the deformation tensor defined as $D_{ij} = (\partial_i u_j + \partial_j u_i)/2$. The Dirac delta function δ_s expresses the fact that the surface-tension coefficient σ is concentrated

on the interface. The radius of curvature of the interface is denoted by κ, and $\boldsymbol{n}$ is the unit outward vector normal to the interface.

A VOF function $c(\boldsymbol{x}, t)$ is introduced to trace the multifluid interface. It is defined as the volume fraction of a given fluid in each cell of the computational mesh. The density and viscosity can thus be written as

$$\rho(\tilde{c}) \equiv \tilde{c}\rho_1 + (1 - \tilde{c})\rho_2 \tag{4}$$

$$\mu(\tilde{c}) \equiv \tilde{c}\mu_1 + (1 - \tilde{c})\mu_2 \tag{5}$$

with ρ_1, ρ_2 and μ_1, μ_2 the densities and viscosities of the first and second fluids, respectively. The field variable $\tilde{c}$ is either identical to c or is constructed by applying a smoothing spatial filter to c. For a high density ratio, the liquid–gas system property change across the interface can lead to strong shear at the interface and cause numerical stability issues. Improved results can be obtained if a smooth field is used to define the density and viscosity. When spatial filtering is implemented, the field $\tilde{c}$ is constructed by averaging the eight (in 3D simulations) cell-corner values of c obtained by bilinear interpolation from the cell-centered values. The properties associated with the interface are subsequently "smeared" over three discretization cells (Popinet, 2003, 2009).

According to mass continuity, the advection equation for the density takes the following form in terms of the volume fraction:

$$\partial_t c + \nabla \cdot (c\boldsymbol{u}) = 0 \tag{6}$$

A staggered temporal discretization of the volume fraction/density and pressure leads to a scheme which is second-order accurate in time (Popinet, 2009). A classical time-splitting projection method (Chorin, 1969) is used, which requires the solution of a Poisson equation. It is well established that standard multigrid schemes exhibit slow convergence for elliptic equations with discontinuous coefficients and stiff source terms, especially for flows with large density ratios. In order to improve numerical efficiency and robustness, the discretized momentum equation is reorganized to a Helmholtz-type equation that can be solved by means of an improved multilevel Poisson solver (Popinet, 2009). The resulting Crank-Nicholson discretization of the viscous terms is second-order accurate and unconditionally stable for a Courant-Friedrichs-Lewy (CFL) number smaller than unity.

Spatial discretization is achieved using a graded Octree partitioning in three dimensions. All the variables are collocated at the center of each discretized cubic volume. Consistent with the finite-volume formulation, variables are interpreted as volume-averaged values for each cell. The choice of a collocated definition of all variables simplifies the enforcement of the momentum conservation when dealing with mesh adaptation (Popinet, 2003).

To solve the advection equation for the volume fraction, Popinet (2009) uses a piecewise-linear geometrical VOF scheme generalized for the Quad/Octree spatial dis-

cretization. The interface is represented in each cell by a line (respective plane in three dimensions) described by the equation $\boldsymbol{m} \cdot \boldsymbol{x} = \alpha$, where $\boldsymbol{m}$ is the local normal to the interface and $\boldsymbol{x}$ is the position vector. For given $\boldsymbol{m}$ and the local volume fraction c, α is uniquely determined by requiring that the volume of fluid contained in the cell and lying below the plane is equal to c. This volume can be computed relatively easily by taking into account the different ways in which a square (resp. cubic) cell can be cut by a line (resp. plane) that leads to matched linear and quadratic (resp. cubic) functions of α.

An accurate estimation of the surface-tension term in the discretized momentum equation represents one of the most difficult aspects of the application of VOF methods to surface-tension-driven flows (Popinet, 2009). The original continuum-surface-force (CSF) approach (Brackbill et al., 1992) is known to suffer from problematic parasitic currents when applied to the case of a stationary droplet in theoretical equilibrium (Popinet and Zaleski, 1999). Similar difficulties are experienced with other methods based on phase-field descriptions of the interface, including level sets and front tracking with distributed surface tension. Popinet (2009) showed that the combination of a balanced-force surface-tension discretization and a height-function curvature estimation is sufficient to circumvent the problem of parasitic currents, provided that the initial nonequilibrium interface allows enough time to relax to its equilibrium shape. Such relaxation typically occurs on a timescale comparable to the characteristic time of viscous dissipation, as expected from physical considerations. Using the above approach, simulation of stationary droplets in theoretical equilibrium shows a second-order convergence rate.

It is relatively straightforward to extend the height-function technique to an Octree spatial discretization, but the results may become inconsistent when the radius of curvature of the interface is less than approximately five times the grid spacing. In these cases, the parabolic fitting technique is used. The transition between the two curvature estimation techniques has been shown to be consistent with overall second-order accuracy.

The entire scheme allows for a spatially and temporally varying resolution. To facilitate numerical implementation, the size of neighboring cells cannot vary by more than a factor of 2 (commonly referred to as restricted Octree). While this may limit the efficiency of adaptation for three-dimensional problems that have a fractal dimension close to two, it should not be an issue for most complex fluid dynamics problems. In contrast to many previous implementations of mesh adaptation for interfacial flows with Eulerian discretization, the present method is not limited to constant resolution along the interface. The efficiency of mesh adaptation can be substantially enhanced, particularly when dealing with reconnections and breakup of interfaces. One of the advantages of the Octree discretization is that mesh refinement or coarsening can be conducted economically at every time-step with minimal impact on the overall performance. Interpolation of quantities on newly refined or coarsened cells is also relatively simple without jeopardizing the conservation properties of momentum and volume fraction (Popinet, 2003). The refinement level of the root cell is set to be zero. The level of its children cells is 1 and so on recursively. A cell of level n has a resolution of 2^n in each coordinate.

For this study we used these schemes as implemented in the free software code Gerris (http://gfs.sf.net/).

3. FLOW CONFIGURATION

Figure 1 shows the flow configuration of concern. Two identical liquid jets impinge against each other, and a thin sheet forms around the intersection of the two jets. The injected liquid is a glycerin–water solution and the ambient gas is air at 1 atm pressure and 298 K temperature. The angle between the jet centerlines 2α is referred to as the impingement angle. The jet dynamics and subsequent atomization can be characterized by two nondimensional parameters: the Weber and Reynolds numbers. They are defined, respectively, as We = $\rho u_j^2 D/\sigma$ and Re = $\rho u_j D/\mu$, where ρ is the liquid density, D the jet diameter, u_j the mean jet velocity, σ the surface tension, and μ the viscosity of the liquid. The size of the computational domain is set to be $50D \times 30D \times 10D$, to eliminate the effect of domain boundaries. The standard outflow condition is set to the domain boundaries. The velocity profiles of the liquid jets are set to be parabolic when Re ≤ 4000 and 1/7 power law when Re > 4000.

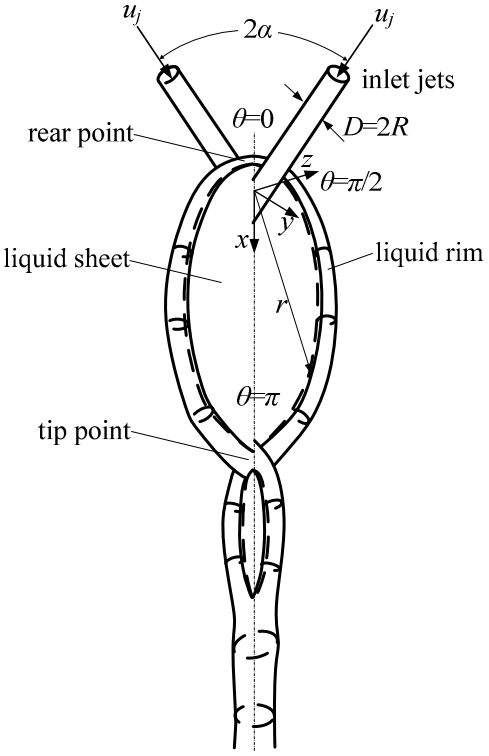

FIG. 1: Schematic diagram of doublet impinging jets.

The present analysis employs an AMR technique with multiple-level resolutions. Several refinement criteria are used concurrently, depending on the physical conditions encountered, to ensure numerical accuracy and robustness. These include gradient-based, value-based, curvature-based, and topology-oriented refinements. The gradient-based criterion guarantees adequate grid refinement on the interface, where VOF has steep gradients, and avoids unnecessary refinement in regions with smooth flow. A fine mesh is required to prevent excessive dissipation of the kinetic energy due to numerical viscosity in situations where it becomes comparable to surface energy. The interior of a specific phase can be refined according to the local VOF value. In the simulation of atomization, the length scale changes dramatically across the computational domain. Fine grids are needed in regions with small length scales in order to resolve topology changes. It is expensive to refine all the interface grids based on the minimum dimension of the liquid. The curvature of the interface can be used to perform curvature-based refinement to resolve the fine regions (Popinet, 2009). In present paper, when curvature-based refinement is used, the condition $\Delta x \kappa_{\max}$ is verified within any cell that contains the interface. Here Δx is cell size and $\kappa_{\max}$ the maximum curvature of the interface in the cell. Since the thickness of a thin region is difficult or expensive to obtain *a priori*, a novel refinement method based on digital topologic theories (Tchon et al., 2005) has been established and implemented to ensure an appropriate number of grid points in the liquid thickness.

Figure 2 shows two examples of adapted interfacial grids with the application of all the aforementioned refinement criteria. For both cases, the jet diameter D is 400 μm, and the impingement angle 2α is 60°. Figure 2(a) presents the simulation results for a low-flow-rate case. The jet velocity u_j is 4.0 m/s. The corresponding Weber and Reynolds numbers are 89.5 and 222.5, respectively. The regions in need of higher refinement include (1) the adjoining area of the liquid rim, (2) the region where the liquid sheet becomes thinner than the remaining area, (3) the rear location where the liquid rim has a small diameter, and (4) the impact zone where the curvature is high. The refinements are achieved according to the geometric characteristics of the rim and sheet formed by impinging jets. Figure 2(b) shows the situation at a higher-flow-rate condition. The jet velocity u_j is 7.9 m/s. The corresponding Weber and Reynolds numbers are 89.5 and 222.5, respectively.

4. GRID REFINEMENT STUDY

4.1 Low-Speed Jets and Stable Sheets

Low-velocity impinging jets are first considered as a benchmark case exhibiting stable liquid sheets, simulating the experiment of Bremond and Villermaux (2006), and shown in Fig. 3. The liquid is a glycerin–water solution, the jet diameter and velocity are 400 μm and 3.3 m/s, respectively, and the impingement angle is 89°. The corresponding

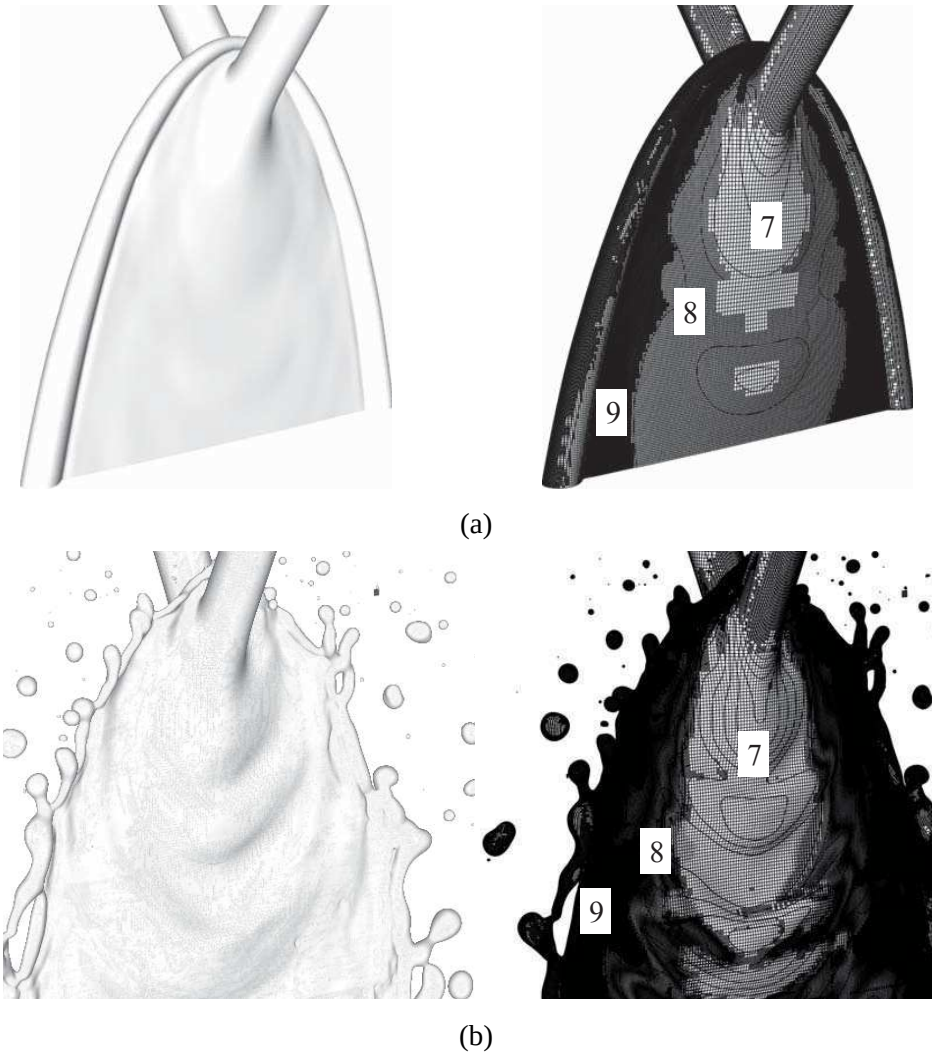

FIG. 2: Flow evolution of impinging jets and interfacial grids obtained by fully AMR simulation: (a) low-speed glycerine–water jets, D = 400 μm, u_j = 4.0 m/s, $2\alpha = 60°$, We = 89.5, Re = 222.5; (b) high-speed glycerine–water jets, D = 400 μm, u_j = 7.9 m/s, $2\alpha = 60°$, We = 343.5, Re = 3536.

Reynolds and Weber numbers are 40.4 and 58.8, respectively. A stable sheet forms under equilibrium among surface tension, centrifugal force, and inertia on the edges of the sheet. Since the stable shape shows a Weber number similarity (Taylor, 1959; Huang, 1970; Clanet and Villermaux, 2002), the experimental data normalized by DWe for the same impingement angle (Bremond and Villermaux, 2006) can be used to validate the simulation results.

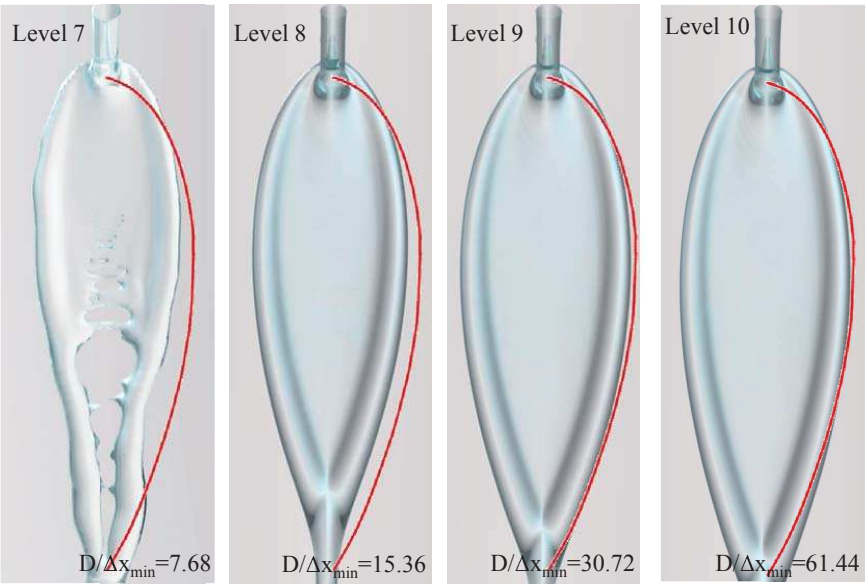

FIG. 3: Numerical simulations of low-velocity impinging jets, where volume rendering has been used to visualize the interface (glycerine–water jets, $D = 400$ μm, $u_j = 3.3$ m/s, $2\alpha = 89°$, We $= 58.8$, Re $= 40.4$).

For impinging jets, the flow around the sheet is uneven. The mass flux is highest in the forward flow direction and smallest in the reverse flow direction. A simple expression for the thickness distribution in undistorted liquid sheets formed by impinging jets was obtained by Hasson and Peck (1964) and is given by

$$\frac{hr}{R^2} = \frac{\sin^3 \alpha}{(1 + \cos \theta \cos \alpha)^2} \tag{7}$$

where h is the sheet thickness, r the radial distance, R the jet radius, α the impingement half-angle, and θ the angular position, as illustrated in Fig. 1. For the forward flow direction at $\theta = 180°$, the thickness parameter hr/R^2 reaches its maximum for a specific impingement angle. For $2\alpha = 89°$, the maximum value of hr/R^2 is 4.30. It is reasonable to assume that at the location where the grid refinement cannot resolve the liquid sheet, the sheet thickness is equal to the minimum grid size. Then the refinement requirement for resolving the sheet can be expressed as $\Delta x/R = 4.30/(r/R)$. The nondimensional expression is $\Delta \bar{x} = 4.30/\bar{r}$. In the present configuration, the grid levels of 7, 8, and 9 are sufficient to resolve the sheet evolution upstream at radial distances of $16.51R$, $33.02R$, and $66.05R$, respectively, as shown in Fig. 3. Table 1 lists the minimum grid sizes for the four different refinement levels. According to the measurement of Bremond and Viller-

TABLE 1: Adaptive mesh refinement levels for the low-velocity case (glycerine–water jets, $D = 400$ μm, $u_j = 3.3$ m/s, $2\alpha = 89°$, We = 58.8, Re = 40.4)

Case no.		Liquid phase	Interface	Gas phase
L1	RL	6	7	5
	$D/\Delta x_{\min}$	3.8	7.7	1.9
L2	RL	7	8	5
	$D/\Delta x_{\min}$	7.7	15.4	1.9
L3	RL	8	9	5
	$D/\Delta x_{\min}$	15.4	30.7	1.9
L4	RL	9	10	5
	$D/\Delta x_{\min}$	30.7	61.4	1.9

*RL = refinement level

maux (2006), the tip location of the rim is at $39.98R$ downstream of the impingement point. The minimum grid level required to capture the thinnest location at the rim tip is 9.

In the four cases considered in the present grid-independence study, only gradient-based and value-based refinement criteria are used. The basic grid level is 5, and the gas phase is resolved with this refinement level. The interfacial resolution is set to be one level higher than that in the liquid phase. Since the flow field is only refined locally using AMR, both computational memory and time are substantially reduced as compared to uniform meshes at the same level of resolution. For example, with the maximum refinement level of 9, only 1,077,182 cells are used, while a total of $(2^9)^3$ = 134,217,728 cells are required for the same resolution with a uniform mesh. Less than 1% of grid points are employed in the present study, as compared to a uniform mesh.

Figure 3 shows front views of the simulation results for the low-velocity case. The rim location measured by Bremond and Villermaux (2006) is shown in red. Realistic ray-tracing rendering is used to visualize the flow development. At a refinement level of 7, the simulation fails to provide an accurate result. This is mainly attributed to the fact that the grid size at the interface is larger than the thickness of the thin film ($h_{\min} =$ 26 μm). Since only one interface is present in a single cell, the liquid sheet cannot sustain the equilibrium and break in the downstream region. At a refinement level of 8, the simulation is able to resolve the entire liquid sheet. This is contrary to the deduction from the above analysis, which showed that the minimum required refinement is level 9. The reason for this disagreement lies in the fact that the calculated sheet length at the refinement level of 8 is much shorter than the experimental value. With higher grid refinement levels of 9 and 10, the calculated shape of the liquid rim agrees with experimental mea-

surements. A small discrepancy between the finest simulation and measurement remains visible, possibly caused by the lack of information about the exact inlet conditions used by Bremond and Villermaux (2006).

Figure 4 shows the interface and mesh at the cross section near the tip of the liquid rim with different grid refinement levels. The result corresponding to level 7 is not shown here, since it cannot resolve the liquid sheet at this location. The smallest number of grid points in the liquid thickness for refinement levels 8, 9, and 10 are 1, 2, and 3, respectively. The above observation indicates that at least one grid in the thickness of the thinnest liquid sheet is required to achieve qualitatively correct results. A quantitatively accurate result requires at least three grid points to resolve the thinnest location. It is worth noting that for the finest resolution, only one quarter of the computational time is needed to obtain the same result if all the aforementioned four AMR criteria are implemented.

4.2 High-Speed Jets and Atomization

Experimental measurements by Ryan et al. (1995) are selected for the grid-independence study of impinging jet atomization for this case. This case involves liquid water jets with $D = 635$ μm and $u_j = 18.1$ m/s. The corresponding Weber and Reynolds numbers are 2860 and 11,748, respectively. Three different grid refinements for the liquid phase

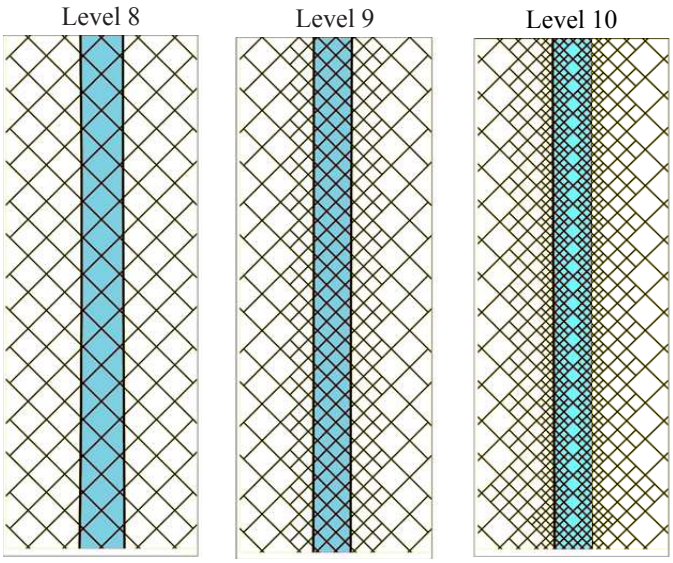

FIG. 4: Interface and mesh cross sections with different combinations of grid refinement levels (glycerine–water jets, $D = 400$ μm, $u_j = 3.3$ m/s, $2\alpha = 89°$, We $= 58.8$, Re $=$ 40.4).

and interface are considered. The base level of the simulation domain is set to be 5 to resolve the gas phase. The refinement of the liquid phase is one level lower than that of the interface. The smallest grid sizes for the three cases are about 83, 41, and 21 μm, with 7.68, 15.36, and 30.72 cells in one jet diameter, respectively. Table 2 gives the grid information in more detail. No turbulence modeling is taken into account, so the analysis can focus on the hydrodynamics of the jets without the complications of model uncertainties. The present study acts as an idealized direct numerical simulation (DNS) of jet impingement and consequent flow development. Since droplets with diameters smaller than the minimum grid size cannot be well resolved, they are removed from the computational domain during the simulation to reduce the numerical cost. These small droplets have minimal effect on the flow field.

Figure 5 shows the simulation results using different refinement levels. With low resolution (level 7), the liquid sheet formed by the two impinging jets cannot be resolved and shows unphysical results, as shown in Fig. 5(a). Since the small droplets are removed, only a few droplets downstream of the impingement point are present. In addition, the formation of flapping waves is not predicted at all. With the medium resolution (level 8) shown in Fig. 5(b), large-amplitude hydrodynamic instabilities, known as impact waves, are clearly observed. The liquid sheet quickly breaks into thick ligaments and large droplets. The high-resolution simulation at level 9, however, can resolve detailed flow structures, including small-scale dynamics of ligaments and droplets, as shown in Fig. 5(c).

Figure 6 shows the numerical grids and interfacial dynamics at the center cross section with different grid refinements. The breakup length increases with increasing grid resolution. A higher-level refinement allows for the resolution of the sheet motion over a longer distance. The impact wavelengths predicted by different grid resolutions are all of the order of one jet diameter; this agrees with the experimental observations of Ryan et al. (1995). The initial wave motion can still be captured, even with the lowest resolution of level 7. As shown in the left image of Fig. 6(b), the mesh in the near

TABLE 2: Adaptive mesh refinement of the high-velocity case (water jets, $D = 635$ μm, $u_j = 18.5$ m/s, $2\alpha = 60°$, We $= 2987$, Re $= 11{,}724$)

Case no.		Liquid phase	Interface	Gas phase
H1	RL	6	7	4
	$D/\Delta x_{\min}$	3.8	7.7	1.0
H2	RL	7	8	4
	$D/\Delta x_{\min}$	7.7	15.4	1.0
H3	RL	8	9	4
	$D/\Delta x_{\min}$	15.4	30.7	1.0

*RL = refinement level

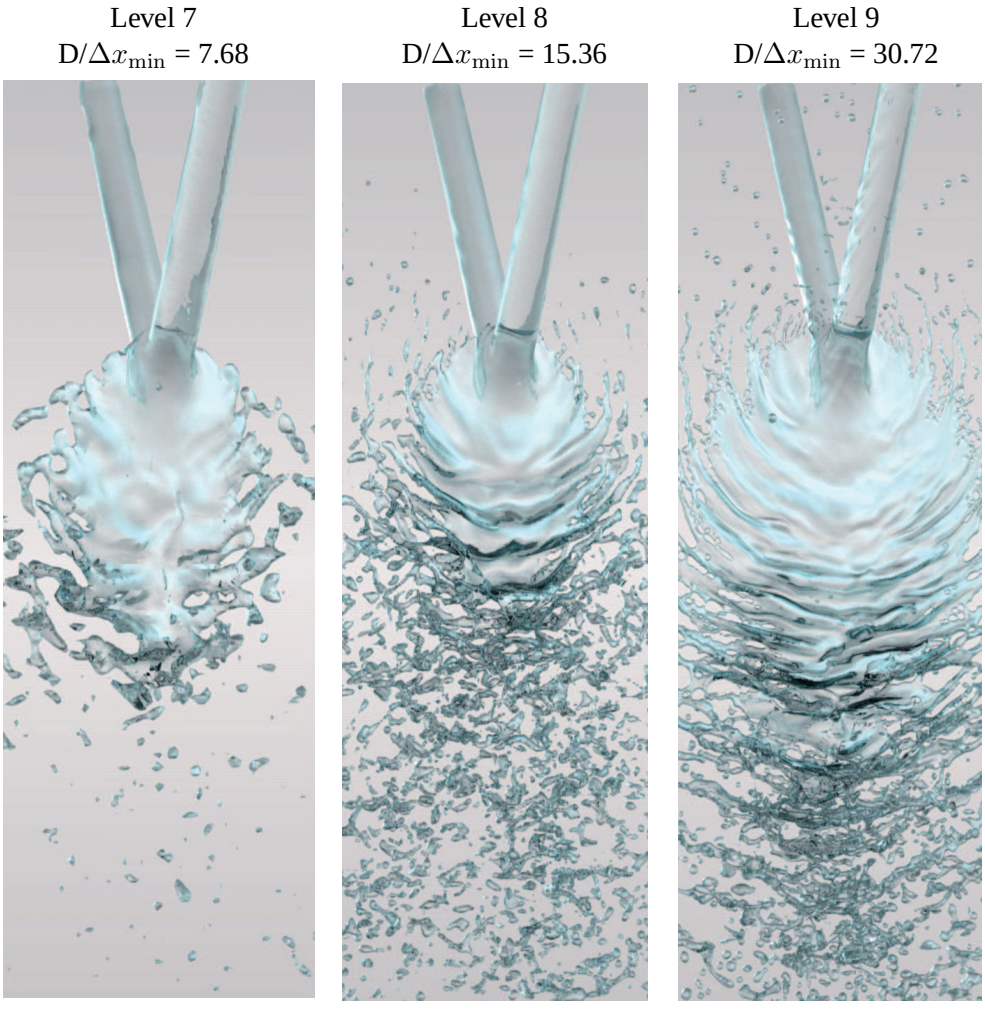

FIG. 5: High-velocity impinging jets (water jets, $D = 635$ μm, $u_j = 18.5$ m/s, $2\alpha = 60°$, We = 2987, Re = 11,724).

field of the liquid sheet looks much finer than that in Fig. 6(c). This is because more droplets than liquid ligaments are formed in the near-field region for the lower refinement level.

Figure 7 shows the probability density function (PDF) of droplet sizes downstream of the impact waves at $x = 21D$. The experimental measurement by Ryan et al. (1995) is also shown in the figure. Since the droplets with diameters smaller than three times the minimum grid size are rejected in the statistics, the starting points of the two curves

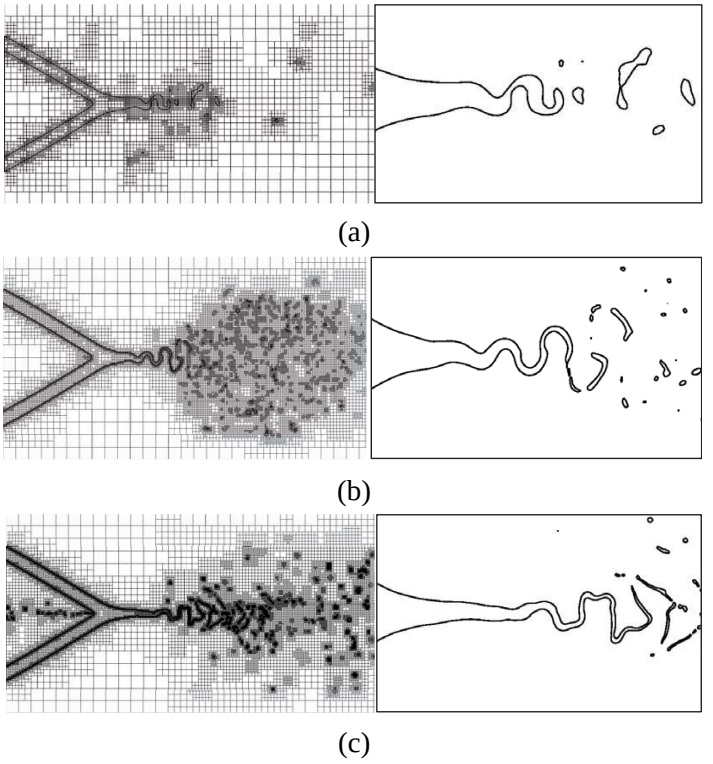

FIG. 6: Numerical grids and interfacial dynamics with different grid resolutions: (a) level 7, (b) level 8, and (c) level 9 (water jets, $D = 635$ μm, $u_j = 18.5$ m/s, $2\alpha = 60°$, We $= 2987$, Re $= 11{,}724$, following).

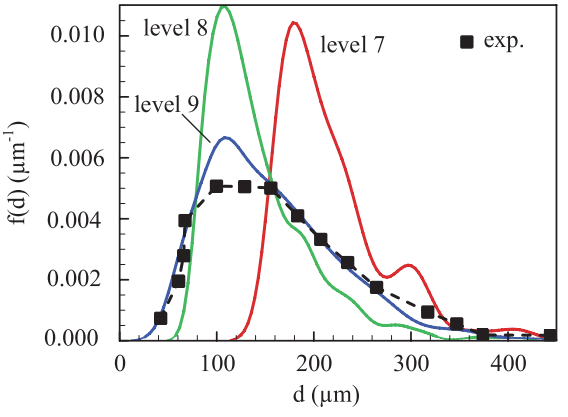

FIG. 7: PDF of droplet sizes at different resolutions compared with experimental data from Ryan et al. (1995) (water jets, $D = 635$ μm, $u_j = 18.5$ m/s, $2\alpha = 60°$, We $= 2987$, Re $= 11{,}724$).

are different and are a function of the minimum cell size. The predicted droplet size distribution agrees well with the measured data at higher resolution. The most probable droplet diameter is 180 μm for the low-resolution case, while the experimental data shows a plateau from 100 to 156 μm. The peak PDF for both the medium- and high-resolution cases corresponds to a droplet size of 108 μm. The high resolution leads to a broader size distribution, a situation that shows good agreement with experimental data. The droplet size varies over a large range: 40–400 μm. The smallest thickness of the liquid sheet is about 21 μm. It is obvious that increasing the refinement level further will lead to better agreement with the experimental data. Since the flow physics was captured satisfactorily with the present grid resolution, however, the costly simulation (run time about two months on 48 processors with 3.0 GHz frequency) of the next refinement level was not performed in the current research effort.

5. FLOW PATTERNS OF IMPINGING JETS

The theoretical and numerical framework outlined in Sec. 2 is used to study the impinging jet dynamics of a glycerin–water solution. The jet diameter is 400 μm, and the impingement angle is fixed at 60°. Figure 8 shows the various flow patterns observed at different jet velocities varying from 2.2 to 11.2 m/s. The different flow patterns are dependent on the Reynolds and Weber numbers. Movies showing the evolution of the liquid rim, sheet, and atomization can be found in Chen and Yang (2012). Figure 8(a) shows a well-defined liquid chain structure at $u_j = 2.2$ m/s. Both a liquid sheet and a closed rim form in the first ring. No sheet, however, exists after the second chain link, due to viscous dissipation and the resultant reduction in the inertial energy of the combined liquid streams. The colliding streams from the two sides of the rim coalesce into a single column oscillating under the inertial-capillary interaction. Finally, breakup takes place at the end of the column because of the plateau Rayleigh instability. As the jet velocity increases, a larger liquid sheet is established, as shown in Fig. 8(b). Since the sheet and rim formed afterward are much smaller, this pattern is usually referred to as a closed rim.

At a higher jet velocity, the liquid sheet becomes unstable, with an oscillating boundary. Figure 8(c) shows a pattern known as a disintegrating sheet. The thin liquid sheet in the downstream region is prone to small disturbances. Holes are formed and grow progressively, eventually reaching the sheet boundary to open the rim. The ligaments downstream of the opening breakup because of capillary action. The disintegrating sheet is also referred to as an open-rim structure. As the jet velocity further increases to 7.9 m/s, the liquid rim becomes unstable, as shown in Fig. 8(d). Disturbances originate at the impingement point and grow, while propagating downstream along the liquid rim. Ligaments are then formed and break up into droplets due to the end-pinching mechanism. In the extreme case of $u_j = 11.2$ m/s, shown in Fig. 8(e), the liquid sheet becomes unstable, with violent flapping, followed by rapid atomization into droplets.

(a) (b) (c)

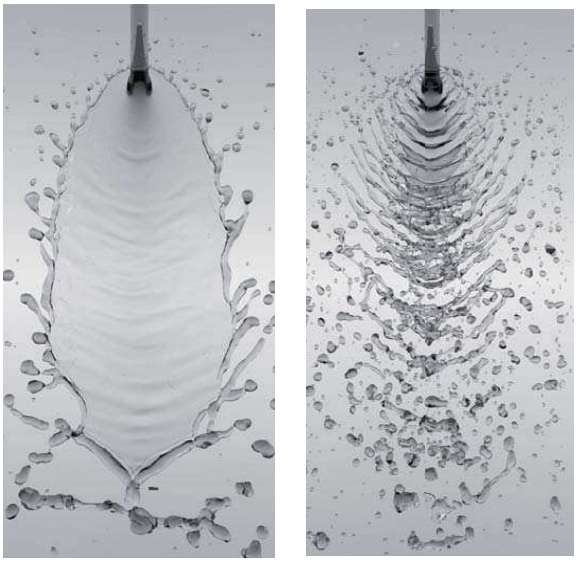

(d) (e)

FIG. 8: Impinging jet flow patterns of glycerin–water solution obtained from simulations [movie showing the flow development can be found in Chen and Yang (2012)], D = 400 μm, $2\alpha = 60^\circ$: (a) liquid chain ($u_j = 2.2$ m/s, We $= 27.5$, Re $= 1000$); (b) closed rim ($u_j = 3.3$ m/s, We $= 58.8$, Re $= 40.4$); (c) open rim ($u_j = 5.3$ m/s, We $= 152$, Re $=$ 294); (d) unstable rim ($u_j = 7.9$ m/s, We $= 343.5$, Re $= 3536$); and (e) impact wave ($u_j = 11.2$ m/s, We $= 687$, Re $= 5000$).

6. IMPACT WAVE DYNAMICS AND ATOMIZATION

For a more detailed view, Fig. 9 shows a snapshot of the impact wave under the flow conditions corresponding to Fig. 8(e). The liquid surface is colored by the z coordinate to show the location with respect to the center plane. The impact waves and ligaments distribute in an interlaced manner on their respective sides of the injected liquid streams. Rupture of the liquid sheet takes place near the rear point, where the thickness is smallest. As indicated by the black arrow, the location of the rupture is between the wave crests and troughs. The discontinuity in the liquid phase created at the rupture point enlarges as the liquid sheet moves downstream. Under the effect of local acceleration introduced by the wave motion, the resultant ligaments are located along the wave crests and troughs and are attached to the flapping liquid sheet. When the openings on the two lateral sides connect, long ligaments are detached from the liquid sheet in the downstream region. The process becomes even more complex as the impact waves interact, resulting in different interference patterns.

Figure 10 shows the spatial distribution of the flow field obtained from the finest simulation in Sec. 4 (level 9) and offers direct insight into the atomization process. The

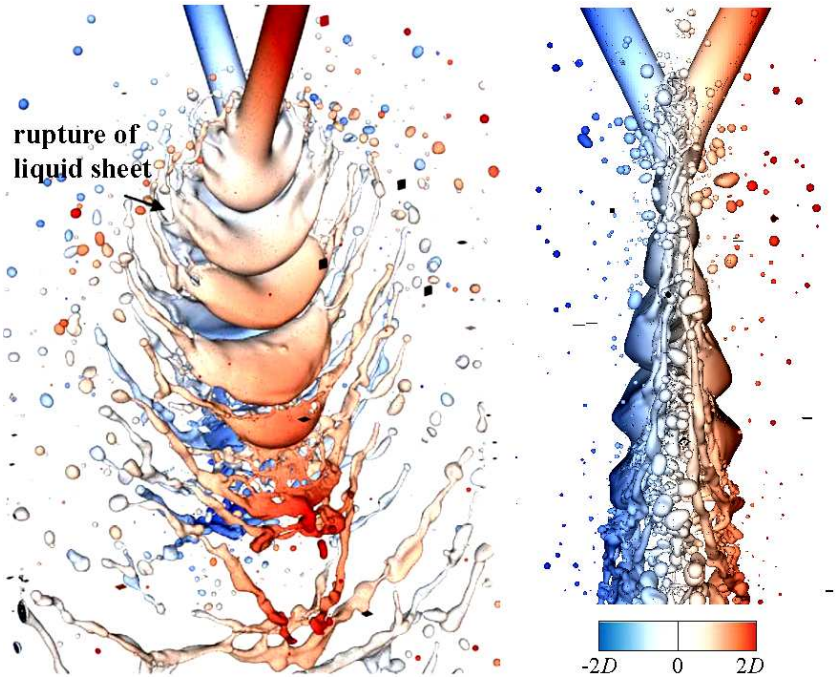

FIG. 9: Detailed image showing the process of ligament formation with interface colored by z coordinate: (a) oblique view and; (b) side view (glycerine–water jets, $D = 400$ μm; $u_j = 11.2$ m/s, $2\alpha = 60°$, We $= 687$, Re $= 5000$).

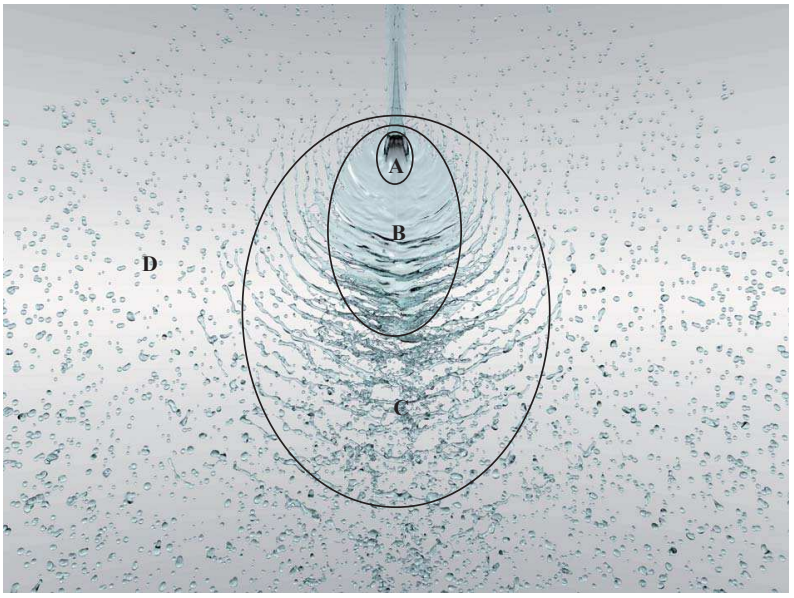

(a)

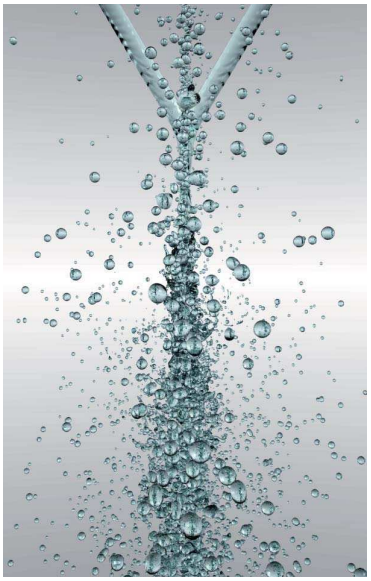

(b)

FIG. 10: Spatial distribution of flow field predicted by level 9 simulation: (a) front view and; (b) side view. Various regions in impinging jet atomization dominated by impact wave: (A) jet impingement region; (B) flapping sheet region; (C) ligament region; and (D) droplet region (water jets, $D = 635$ μm, $u_j = 18.5$ m/s, $2\alpha = 60°$, We $= 2987$, Re $=$ 11,724).

liquid jet velocity is 18.5 m/s. The corresponding Weber and Reynolds numbers are 2860 and 11,748, respectively. As shown in Fig. 10(a), the entire flow evolution can be divided into four regions: jet impingement, flapping sheet, ligaments, and droplets. The impact waves arising from hydrodynamic instabilities generate high-amplitude disturbances and cause the sheet to fragment. The collision of the two liquid jets in region A forms a liquid sheet expanding from the impingement point. The sheet thickness is uneven because of the nonuniform velocity profiles of the incoming streams. In region B, impact waves are generated and propagate radially outward from the impingement point. The liquid sheet is then ruptured by the impact wave and breaks along the waves to form arc-shaped structures in region C. Capillary instabilities further cause the ligaments to break up, as shown in region D. In general, the droplet and ligament sizes decrease radially outward from the core.

Figure 11 shows the velocity profiles at different axial locations near the impingement point, where $y = 0$ corresponds to the centerline of the liquid stream. The flow condition is identical to that shown in Fig. 10. The inlet velocity profile at location 1 is set to $8/7(1 - x/D)^{1/7}u_j$. Since location 2 is near the impingement point, the velocity is lowest at the center. Further downstream, the velocity at the center increases. The velocity profile shows a parabolic profile at location 4 just before the formation of the impact wave. As observed by Sander and Weigand (2008), the mean velocity profile has a profound effect on the stability characteristics. A single liquid sheet with a parabolic velocity profile at the entrance exhibits a flapping pattern similar to the one observed in the present case of an impinging-jet-formed sheet.

The impact wave also exists at low-Weber-number conditions but has damped amplitude, as shown in Fig. 8(d). The wave propagation frequency can be expressed as $f = u_s/\lambda$, where u_s is the characteristic velocity of the liquid sheet and λ the wavelength. The Strouhal number for the impact wave can thus be defined as $\mathrm{St} = fD/u_s = D/\lambda$. Figure 12 shows the dependence of the relationship between the Strouhal and the Weber number with $2\alpha = 60^\circ$. The Strouhal number increases linearly with increasing Weber number. It levels off at a constant value of about 0.835 for $\mathrm{We} > 1000$. The same phenomenon has been observed in studies on perturbed free shear layers (Drubka, 1981; Kibens, 1981; Ho and Hsiao, 1983). This suggests that the flow mechanism of impact wave is analogous to that of free shear layers. As suggested by the vorticity profiles given in Fig. 11, the combination of two shear layers with opposite vorticity directions exhibits behaviors resembling those of a single shear layer with a parabolic velocity profile. The interaction between the two shear layers is the primary cause of the wave dynamics after jet impingement.

7. CONCLUSIONS

A high-fidelity numerical framework has been developed and implemented to study the dynamics of the liquid sheets formed by two impinging jets. The work employs a three-

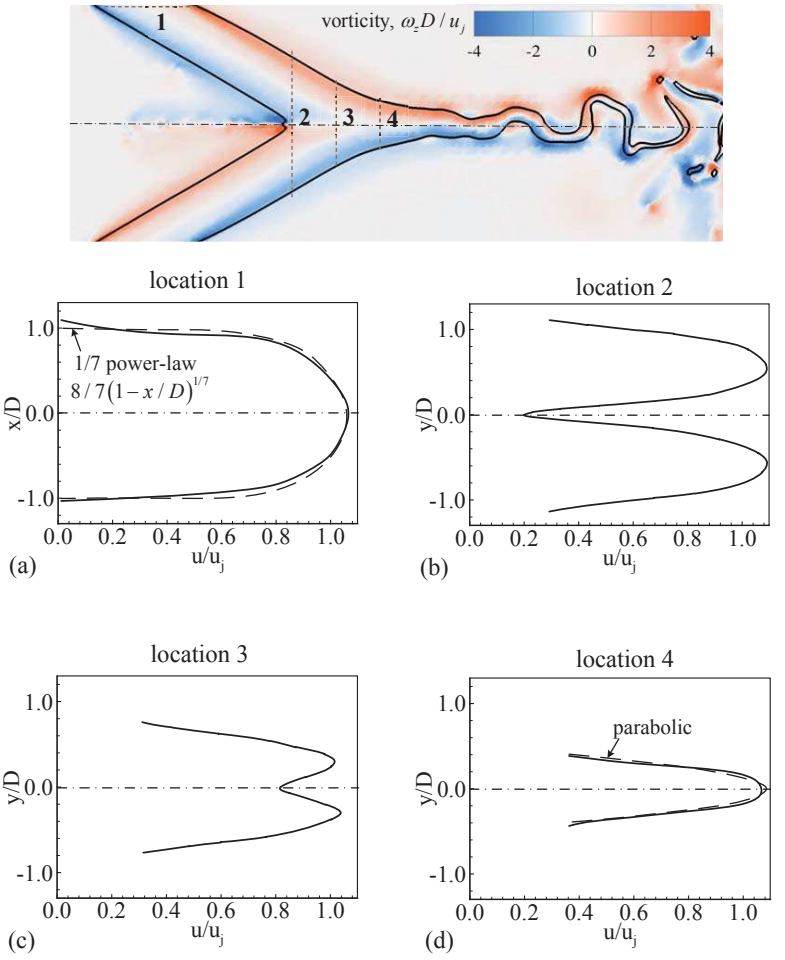

FIG. 11: Evolution of velocity profiles near impingement point (water jets, $D = 635$ μm, $u_j = 18.5$ m/s, $2\alpha = 60°$, We $= 2987$, Re $= 11{,}724$).

dimensional volume-of-fluid (VOF) method with adaptive mesh refinement (AMR) based on Octree meshes. Detailed flow physics is explored and compared with experimental data over a wide range of Reynolds and Weber numbers. The temporal evolution and spatial development of the injected liquid, including the jet impingement, sheet formation and rupture, and atomization into ligaments and droplets, are examined in detail. A variety of sheet and atomization patterns formed under different operation conditions are identified. In particular, the underlying mechanisms dictating the behaviors of impact waves are discussed systematically. A new understanding of the primary atomization of impinging jets has been achieved. The numerical scheme developed here provides a self-consistent approach for treating complex interfacial flows with multiple scales.

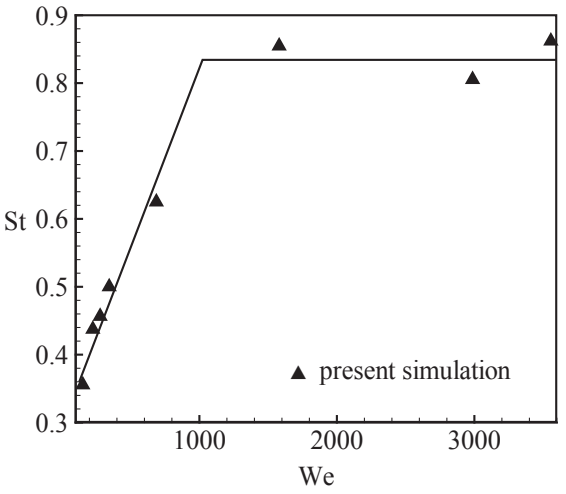

FIG. 12: Strouhal number of impact wave with different Weber numbers.

ACKNOWLEDGMENTS

This work was sponsored by the US Army Research Office under the Multi-University Research Initiative under Contract No. W911NF-08-1-0124. The support and encouragement of Dr. Ralph Anthenien are gratefully acknowledged.

REFERENCES

Arienti, M., Li, X., Soteriou, M., Eckett, C., Sussman, M., and Jensen, R., Coupled level-set/volume-of-fluid method for simulation of injector atomization, *J. Propul. Power*, vol. **29**, no. 1, pp. 147–157, 2013.

Bayvel, L. and Orzechowski, Z., *Liquid Atomization*, CRC Press, vol. 1040, Boca Raton, FL, 1993.

Brackbill, J., Kothe, D., and Zemach, C., A continuum method for modeling surface tension, *J. Comput. Phys.*, vol. **100**, no. 2, pp. 335–354, 1992.

Bremond, N. and Villermaux, E., Atomization by jet impact, *J. Fluid Mech.*, vol. **549**, no. 1, pp. 273–306, 2006.

Bush, J. W. M. and Hasha, A. E., On the collision of laminar jets: Fluid chains and fishbones, *J. Fluid Mech.*, vol. **511**, pp. 285–310, 2004.

Chen, X. and Yang, V., Impinging jet dynamics, arXiv:1210.3892, 2012.

Choo, Y. and Kang, B., A study on the velocity characteristics of the liquid elements produced by two impinging jets, *Exp. Fluids*, vol. **34**, no. 6, pp. 655–661, 2003.

Choo, Y. and Kang, B., The effect of jet velocity profile on the characteristics of thickness and velocity of the liquid sheet formed by two impinging jets, *Phys. Fluids*, vol. **19**, no. 11, pp. 112101–112107, 2007.

Chorin, A., On the convergence of discrete approximations to the Navier-Stokes equations, *Math. Comput.*, vol. **23**, no. 106, pp. 341–353, 1969.

Clanet, C. and Villermaux, E., Life of a smooth liquid sheet, *J. Fluid Mech.*, vol. **462**, no. 1, pp. 307–340, 2002.

Dombrowski, N. and Hooper, P., A study of the sprays formed by impinging jets in laminar and turbulent flow, *J. Fluid Mech.*, vol. **18**, no. 3, pp. 392–400, 1963.

Drubka, R. E., *Instabilities in Near Field of Turbulent Jets and Their Dependence on Initial Conditions and Reynolds Number*, Illinois Institute of Technology, Chicago, IL, 1981.

Hasson, D. and Peck, R. E., Thickness distribution in a sheet formed by impinging jets, *AIChE J.*, vol. **10**, no. 5, pp. 752–754, 1964.

Heidmann, M. F., Priem, R. J., Humphrey, J. C., and Center, N. G. R., *A Study of Sprays Formed by Two Impinging Jets*, National Advisory Committee for Aeronautics, 1957.

Ho, C. M. and Hsiao, F. B., *Structure of Complex Turbulent Shear Flow*, Dumas, R. and Fulachier, L., eds., Chap. 4, Evolution of coherent structures in a lip jet, p. 121, Springer Verlag, Berlin, 1983.

Huang, J., The break-up of axisymmetric liquid sheets, *J. Fluid Mech.*, vol. **43**, no. 2, pp. 305–319, 1970.

Ibrahim, E. and Przekwas, A., Impinging jets atomization, *Phys. Fluids A*, vol. **3**, p. 2981, 1991.

Inoue, C., Watanabe, T., and Himeno, T., Study on atomization process of liquid sheet formed by impinging jets, AIAA Paper no. 2008-4847, 2008.

Inoue, C., Watanabe, T., and Himeno, T., Liquid sheet dynamics and primary breakup characteristics at impingement type injector, AIAA Paper no. 2009-5041, 2009.

Jung, S., Hoath, S. D., Martin, G. D., and Hutchings, I. M., Atomization patterns produced by the oblique collision of two newtonian liquid jets, *Phys. Fluids*, vol. **22**, p. 042101, 2010.

Kang, B., Shen, Y., and Poulikakos, D., Holography experiments in the breakup region of a liquid sheet formed by two impinging jets, *Atomization Sprays*, vol. **5**, no. 4, pp. 387–402, 1995.

Kibens, V., The limit of initial shear layer influence on jet development, *AIAA J.*, vol. **81**, p. 19, 1981.

Lefebvre, A. H., *Atomization and Sprays*, CRC Press, Boca Raton, FL, 1989.

Li, R. and Ashgriz, N., Characteristics of liquid sheets formed by two impinging jets, *Phys. Fluids*, vol. **18**, p. 087104, 2006.

Lin, S. P., *Breakup of Liquid Sheets and Jets*, Cambridge University Press, Cambridge, England, 2003.

Oefelin, J. C. and Yang, V., Comprehensive review of liquid-propellant combustion instabilities in F-1 engines, *J. Propul. Power*, vol. **9**, no. 5, pp. 657–677, 1993.

Popinet, S., Gerris: A tree-based adaptive solver for the incompressible Euler equations in complex geometries, *J. Comput. Phys.*, vol. **190**, no. 2, pp. 572–600, 2003.

Popinet, S., An accurate adaptive solver for surface-tension-driven interfacial flows, *J. Comput. Phys.*, vol. **228**, no. 16, pp. 5838–5866, 2009.

Popinet, S. and Zaleski, S., A front-tracking algorithm for accurate representation of surface tension, *Int. J. Numer. Methods Fluids*, vol. **30**, no. 6, pp. 775–793, 1999.

Ryan, H., Anderson, W., Pal, S., and Santoro, R., Atomization characteristics of impinging liquid jets, *J. Propul. Power*, vol. **11**, no. 1, pp. 135–145, 1995.

Sander, W. and Weigand, B., Direct numerical simulation and analysis of instability enhancing parameters in liquid sheets at moderate Reynolds numbers, *Phys. Fluids*, vol. **20**, p. 053301, 2008.

Shen, Y. B. and Poulikakos, D., Thickness variation of a liquid sheet formed by two impinging jets using holographic interferometry, *J. Fluids Eng.*, vol. **120**, p. 482, 1998.

Sussman, M., Smith, K., Hussaini, M., Ohta, M., and Zhi-Wei, R., A sharp interface method for incompressible two-phase flows, *J. Comput. Phys.*, vol. **221**, no. 2, pp. 469–505, 2007.

Sutton, G. P. and Biblarz, O., *Rocket Propulsion Elements*, Wiley, New York, 2011.

Taylor, G., The dynamics of thin sheets of fluid, III. Disintegration of fluid sheets, *Proc. R. Soc. London, Ser. A*, vol. **253**, no. 1274, pp. 313–321, 1959.

Taylor, G., Formation of thin flat sheets of water, *Proc. R. Soc. London, Ser. A*, vol. **259**, no. 1296, pp. 1–17, 1960.

Tchon, K. F., Khachan, M., Guibault, F., and Camarero, R., Three-dimensional anisotropic geometric metrics based on local domain curvature and thickness, *Comput.-Aided Des.*, vol. **37**, no. 2, pp. 173–187, 2005.

Yang, V. and Anderson, W., Liquid rocket engine combustion instability: Progress in Astronautics and Aeronautics, vol. 196, AIAA, 1995.